The migration and occupation of Li^+ and Na^+ in illite and montmorillonite during the heating process

Zhenxiao Wu[1], Shangying Li[1,2], Yang Wang[1] and Hongfei Cheng [1]*

[1]School of Earth Science and Resources, Chang'an University, No. 126 Yanta Road, Xi'an 710054, China; and [2]School of Land Engineering, Chang'an University, No. 126 Yanta Road, Xi'an 710054, China

Abstract

The impact of temperature on the migration of cations within layers of clay minerals is of profound significance for the design and practical application of materials derived from clay minerals. This study focuses on Li^+ and Na^+ as representative cations, and employs illite (Ilt) and montmorillonite (Mnt) as representative clay minerals. The study investigates the behavior of cation migration and occupation within clay minerals across varying temperatures. A series of samples were meticulously prepared by immersing Ilt and Mnt in Li^+ and Na^+ solutions, subsequently subjecting them to different temperatures (unheated, 100, 150, 200, 250, and 300 °C) for 24 h. Through the use of techniques such as X–ray diffraction (XRD), cation exchange capacity (CEC), Fourier transform infrared spectroscopy (FTIR), magic angle rotating solid nuclear magnetic resonance spectroscopy (MAS NMR), and X–ray photoelectron spectroscopy (XPS), the study discerns structural transformations in Ilt and

***Corresponding author:** Hongfei Cheng; Email: h.cheng@chd.edu.cn

This is a 'preproof' accepted article for Mineralogical Magazine. This version may be subject to change during the production process.
DOI: 10.1180/mgm.2024.27

Mnt, and tracks the migration and occupation of Li^+ and Na^+. The findings elucidate that following heating, Na^+ and Li^+ do not infiltrate the lattice of Ilt. In contrast, Na^+ do not migrate into the Mnt lattice, while Li^+ exhibit migration into this lattice. Notably, the migration and occupation of interlayer Li^+ within Mnt exhibit discernible temperature dependence. Specifically, upon reaching 150 °C, interlayer Li^+ migrate to ditrigonal cavities within the tetrahedral layers. As the temperature elevate to 200 °C, Li^+ further permeate vacant octahedral sites through the ditrigonal cavities, culminating in the formation of a localized trioctahedral structure.

Keywords: montmorillonite, illite, Li^+, Na^+, cation migration, cation occupation

(Received 14 December 2023)

https://doi.org/10.1180/mgm.2024.27 Published online by Cambridge University Press

Introduction

Clay minerals have diverse applications across fields, including agriculture, medicine, and the environment, with a notable role as repositories for radioactive waste storage (Komadel *et al.*, 2005; Madejová *et al.*, 2006; Zhao *et al.*, 2022a). Most clay minerals assume a layered silicate structure, and these layers can be categorized as 1:1 and 2:1 type (Cheng *et al.*, 2010; Li *et al.*, 2022). The 1:1 type includes one tetrahedral sheet and one octahedral sheet (Cao *et al.*, 2021), while the 2:1 type includes two tetrahedral sheets with one octahedral sheet situated between them (Bodart *et al.*, 2018). Octahedrons come in two forms: (1) dioctahedral, wherein two thirds of the octahedral cation centers are occupied by cations, and (2) trioctahedral, where all octahedral cation positions are filled (Gao, 2017; Wu *et al.*, 2022). Both illite (Ilt) and montmorillonite (Mnt) are representative 2:1 layer clay minerals displaying dioctahedral structures (Gournis *et al.*, 2008; Zhao *et al.*, 2022b). Negative charges within the structural layer of Ilt and Mnt originate from isomorphous substitution of Al^{3+} in octahedral sheet by Fe^{2+}, Mg^{2+}, etc., alongside limited Al^{3+} replacement for Si^{4+} in tetrahedral sheets. The resulting negative charge is offset by exchangeable cations (*e.g.* Na^{+} and K^{+}) at sheet edges and within interlayers (Chen and Wang, 2007; Wang *et al.*, 2011; Jeldres *et al.*, 2019; Zhao *et al.*, 2022b).

Accurate comprehension of the interaction mechanism between

https://doi.org/10.1180/mgm.2024.27 Published online by Cambridge University Press

mineral lattices and interlayer cations subsequent to heat or hydrothermal treatment is crucial for designing and employing clay mineral–based materials, particularly in radioactive waste storage. Elevated temperatures prompt some interlayer cations to infiltrate clay structures, inducing mineral structural layer collapse and a significant reduction in containment efficacy for radioactive waste (Theng *et al.*, 1997; Alba *et al.*, 1998). Studies reveal that heating clay minerals within the range of 200–300 °C can result in interlayer cation immobilization, leading to irreparable mineral structural layer collapse, known as the Hofmann–Klemen effect (Schultz, 1969; Greene-Kelly, 1995). Three viewpoints exist regarding interlayer cation occupation sites within the Hofmann–Klemen effect: (i) cations infiltrate ditrigonal cavities in tetrahedral layers (Tettenhorst, 1962; Beaufort *et al.*, 2001; Bodart *et al.*, 2018); (ii) cations inhabit vacant octahedral positions (Farmer and Russell, 1967; Gates *et al.*, 2000; Stackhouse and Coveney, 2002); (iii) cations migrate to both sites (Russell and Farmer, 1964; Komadel *et al.*, 2005) (Fig. 1). Notably, research on Mnt heating reveals frequent investigations into interlayer cation migration locations (Karakassides *et al.*, 1999; Madejová *et al.*, 1999a). Based on infrared spectroscopy, Tettenhorst (1962) observed interlayer Li^+ migration into ditrigonal cavities within tetrahedral layers upon Mnt heating to 300 °C, with no migration into vacant octahedra. Luca and Cardile (1988) employed

https://doi.org/10.1180/mgm.2024.27 Published online by Cambridge University Press

a ^{57}Fe atomic probe to ascertain that Li^+ primarily occupied tetrahedral sites during Mnt heating. Infrared spectroscopy-based findings by Farmer and Russell (1967) indicated Li^+ migration into vacant octahedral positions during heating, with remaining interlayer Li^+ interacting with structural OH groups to release H^+. DFT calculations by Ebina *et al.* (1999) postulated interlayer Li^+ migration from interlayers into ditrigonal cavities and vacant octahedral positions in Mnt, occurring at temperatures of 250–350 °C, with respective migration rates of 60% and 40%. Furthermore, studies have reported cation migration during Mnt heating for other cations (e.g., Cd^{2+}, Mg^{2+}, Cu^{2+}, and Ni^{2+}). Based on infrared spectroscopy, Madejová *et al.* (1999b) investigated Cu^{2+} and Cd^{2+} migration between Mnt layers after heating, revealing Cd^{2+} incapability to migrate to tetrahedral and octahedral structures, and Cu^{2+} limited migration into ditrigonal cavities within tetrahedral layers, without further penetration into vacant octahedral positions. It is evident that cationic properties, including ionic radius and valence, significantly impact cation migration sites in clay minerals. Moreover, mineral species can also influence cation transport patterns between layers. However, few studies have examined interlayer cation occupation in distinct clay mineral types following heating. Thus, this study selects Li^+ and Na^+ as representative cations and employs Ilt and Mnt as representative clay minerals. The thermal migration and

https://doi.org/10.1180/mgm.2024.27 Published online by Cambridge University Press

occupation characteristics of interlayer cations in clay minerals were investigated using X–ray diffraction (XRD), Fourier transform infrared spectroscopy (FTIR), magic angle rotating solid nuclear magnetic resonance spectroscopy (MAS NMR), and X–ray photoelectron spectroscopy (XPS).

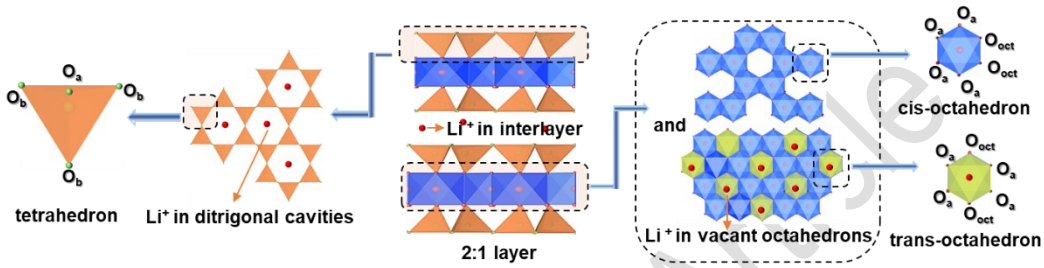

Figure 1. Schematic diagram of occupation sites of Li^+ in clay minerals (Bodart *et al.*, 2018; Zhao *et al.*, 2023).

Experimental

Materials

For this investigation, Ilt and Mnt were selected as the clay minerals under study. Ilt was obtained from the Carboniferous Benxi Formation, located in Kou Town, Xianyang City, Shaanxi Province, while Mnt was procured from Xianding Biotechnology Co. Ltd. To eliminate soluble impurities, the clay mineral samples underwent a thorough process of triple rinsing using deionized water. Subsequently, they were dried in an oven at 50 °C for 24 h and further ground in an agate mortar until reaching a powder consistency with a particle size of 200 mesh. The Na^+ and Li^+ solutions were

https://doi.org/10.1180/mgm.2024.27 Published online by Cambridge University Press

prepared by dissolving Na_2SO_4 and Li_2SO_4 in ultrapure water, respectively. The Na_2SO_4 and Li_2SO_4 of analytical grade were purchased from Tianli chemical reagent Co., Ltd. (Tianjin, China) and Komio Chemical Reagents Co., Ltd (Tianjin, China), respectively. To prepare Na^+–saturated Mnt and Li^+–saturated Mnt (Na^+–Mnt and Li^+–Mnt), 4.00 g of Mnt was added to 100 mL of Na^+ (1M) and Li^+ (1M) solutions, respectively. These solutions were agitated for a duration of 2 h at 25 °C and 50 r/min. Subsequently, the samples underwent centrifugation at 10,000 rpm for 10 min to facilitate solid–liquid separation. The isolated solids were air–dried under natural conditions at ~25 °C. The dried Mnt samples were then exposed to various temperatures for 24 h. The resulting specimens were designated as M–Mnt25, M–Mnt100, M–Mnt150, M–Mnt200, M–Mnt250, and M–Mnt300. In this nomenclature, M signifies either Na^+ or Li^+, M–Mnt25 denotes a sample that was not subjected to heating, and M–Mnt100 signifies a sample heated to 100 °C. Additionally, control samples were produced by mixing 4.00 grams of Ilt with 100 mL solutions of Na^+ (1M) and Li^+ (1M), respectively. The resulting control samples were named M–Ilt25, M–Ilt100, M–Ilt150, M–Ilt200, M–Ilt250, and M–Ilt300.

Characterizations

The major chemical compositions of Ilt and Mnt were analyzed using an X-ray fluorescence spectrometer (XRF, Shimadzu LAB CENTER XRF-1800).

https://doi.org/10.1180/mgm.2024.27 Published online by Cambridge University Press

Cation exchange capacities (CEC) in samples were determined by extraction with ammonium acetate solution (1M) at pH 7. 100 mg sample was rinsed triple with deionized water to remove water-soluble cations and collect solid. The solid was dispersed in 20 mL ethanol, then 20 mL ammonium acetate solution was added, and the extraction solution was collected after standing for 24 h. Subsequently, 20 mL deionized water was added to the remaining solid and the extraction solution was collected after 24 h. The extraction process was repeated three times, and all extraction solutions of the same sample were mixed. The cation concentration (Na^+ and Li^+) in the solution was determined by inductively coupled plasma optical emission spectrometer (ICP-OES, Agilent 5110).

XRD patterns were obtained using a Shimadzu XRD–6100 powder diffractometer. The instrument employed a Cu target as the source (40 kV voltage, 30 mA current) and scanned within the 2θ range of 2–70° at a scanning speed of 4°/min. FTIR spectra were acquired through the KBr pressing method. A Thermo Fisher Nicolet iS5 FTIR spectrometer was employed for data collection, utilizing 1 mg of sample powder and 100 mg of spectrographic pure KBr powder. This mixture was ground thoroughly for 15 min and subsequently pressed into transparent flakes. Infrared spectral data were gathered across the range of 4000–400 cm^{-1}, involving 32 scans at a resolution of 4 cm^{-1}. MAS NMR spectral data for ^{27}Al, ^{29}Si, and

https://doi.org/10.1180/mgm.2024.27 Published online by Cambridge University Press

^{7}Li were obtained using a JEOL ECZ600R/S3 NMR spectrometer from JEOL RESONANCE, Japan. Resonance frequencies were 156.39 MHz for ^{27}Al, 119.20 MHz for ^{29}Si, and 233.08 MHz for ^{7}Li. Single–pulse decoupled MAS NMR experiments were conducted with a 3.2 mm dual resonance probe, employing magic angle rotation speeds of 15 kHz for ^{27}Al, 12 kHz for ^{29}Si, and 8 kHz for ^{7}Li. The pulse widths for ^{27}Al, ^{29}Si, and ^{7}Li were set at π/6, π/2, and π/4, respectively, with corresponding pulse delays. Chemical shifts for ^{27}Al, ^{29}Si, and ^{7}Li were externally referenced to solutions of aluminum nitrate ($Al(NO_3)_3$), tetramethylsilane (TMS), and lithium chloride (LiCl), respectively. XPS was conducted using a Thermo Fisher Scientific ESCALAB Xi+ X–ray photoelectron spectrometer, equipped with a monochromatized Al *K*α X–ray source. The full-spectral pass energy is 100 eV with a step size of 1 eV, and the narrow-spectral pass energy is 30 eV with a step size of 0.1 eV. Typical elements Al, Si, and Li were examined in this study.

Results and Discussion

XRD

The XRD patterns demonstrate the high purity of Ilt and Mnt samples (Fig. 2, Supplementary Fig. S1). Generally, the d values of the 00*l* reflections in minerals are influenced by the radius and hydration status of interlayer cations, while the *hkl* reflections are influenced by mineral layer structure

https://doi.org/10.1180/mgm.2024.27 Published online by Cambridge University Press

(Alvero *et al.*, 1994; Alba *et al.*, 1998). The positions and intensities of *hkl* reflections for Ilt and Mnt, heated to different temperatures, remain consistent with their unheated counterparts (Fig. 2). This indicates the absence of changes in the crystal structure of these minerals. The 00*l* reflections for Ilt show little change upon varying temperatures. In contrast, the 00*l* reflections for Mnt display significant shifts after exposure to different temperatures.

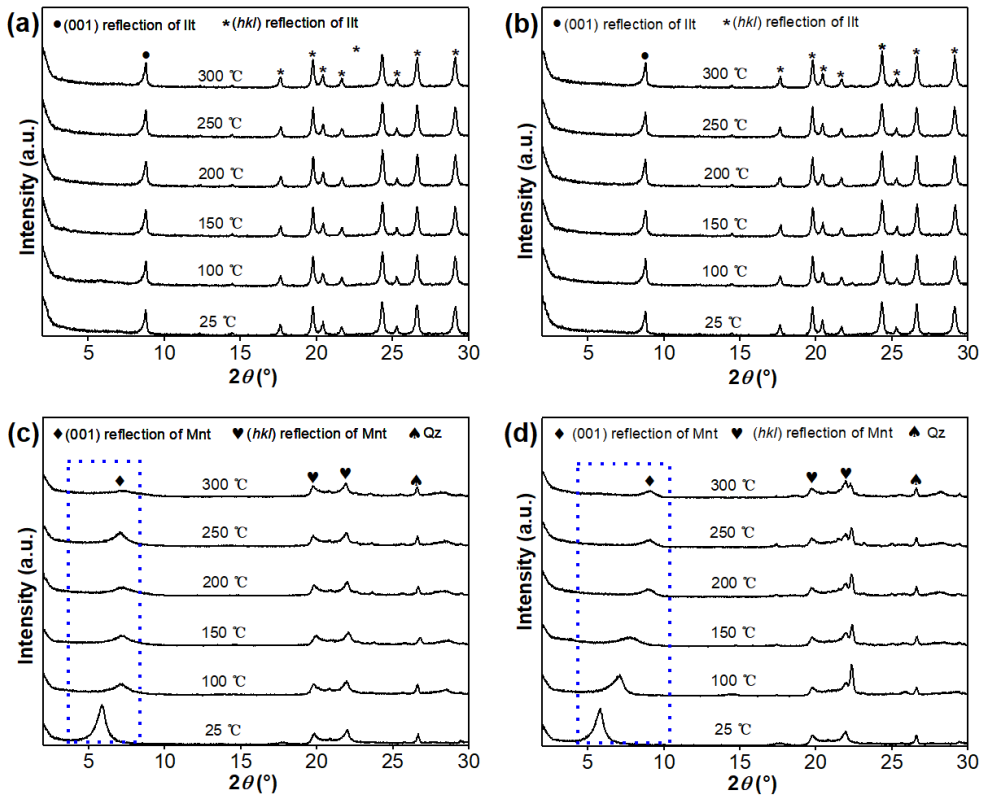

Figure 2. XRD patterns of M-Ilt and M-Mnt subjected to varying temperatures: (a) Na^+–Ilt at different temperatures; (b) Li^+–Ilt at different temperatures; (c) Na^+–Mnt at different temperatures; (d) Li^+–Mnt at different temperatures.

For Ilt, the $d_{(001)}$ value remains ~10.0 Å before and after heating, implying that the hydration status and migration behavior of interlayer

https://doi.org/10.1180/mgm.2024.27 Published online by Cambridge University Press

cations in Ilt are not affected by temperature (Fig. 2a,b) (Jeldres *et al.*, 2019). In the case of Mnt, the layer spacing of Na^+–saturated Mnt (~15.3 Å) is slightly larger than that of Li^+–saturated Mnt (~14.9 Å) in the unheated state. This difference can be attributed to the lower hydration level of Li^+ compared to Na^+, resulting in slightly larger layer spacing when Na^+ occupies the interlayer. The d values of 00*l* reflections for Mnt experience noticeable alterations after exposure to varying temperatures, with a decrease observed in d values as temperature increases (Fig. 2c,d). This may be due to interlayer cations losing ligand water and/or migrating into the Mnt lattice. Specifically, for Na^+–saturated Mnt, the $d_{(001)}$ values decrease to ~12.5, ~12.4, ~12.4, ~12.4, and ~12.4 Å, while for Li^+–saturate Mnt, the values decrease to approximately ~12.4, ~10.9, ~9.9, ~9.6, and ~9.6 Å after heating to 100, 150, 200, 250, and 300 °C respectively. At 200 °C, the layer spacing of Li^+–saturated Mnt falls below 10.0 Å, aligning with the $d_{(001)}$ value for completely collapsed Mnt. Conversely, Na^+–saturated Mnt maintains a layer spacing exceeding 10.0 Å after exposure to varying temperatures, indicating that heating does not lead to complete crystal structure collapse. Electrostatic interaction exists between silicon–aluminate layers and interlayer cations. Heating can prompt interlayer cations to infiltrate mineral crystal structures, resulting in reduced structural layer negativity, low electrostatic repulsion between layers, and

https://doi.org/10.1180/mgm.2024.27 Published online by Cambridge University Press

decreased layer spacing. The extent of decrease in $d_{(001)}$ value suggests that Li^+ exhibits more readiness to infiltrate Mnt crystal structures compared to Na^+.

XRF and CEC

The main chemical compositions of Ilt and Mnt are SiO_2 and Al_2O_3, ranging from 45.8 to 59.5 *wt.*%, and from 25.7 to 36.1 *wt.*%, respectively (Table 1). In addition, the K_2O content in Ilt is higher than that in Mnt. By contrast, the contents of TFe_2O_3 and MgO in Ilt are lower than that in Mnt.

Table 1. Major chemical compositions (*wt.*%) of Ilt and Mnt samples.

Sample	SiO_2	Al_2O_3	TiO_2	TFe_2O_3	MnO	MgO	CaO	Na_2O	K_2O	P_2O_5	LOI
Ilt	45.8	36.1	1.5	1.0	<0.1	0.5	0.4	<0.1	8.5	<0.1	6.9
Mnt	59.5	25.7	<0.1	4.7	<0.1	3.9	1.5	0.9	0.6	<0.1	1.7

The CEC of Na^+ and Li^+ in M–Ilt and M–Mnt are shown in Table 2. The amount of exchangeable Na^+ and Li^+ in Ilt is lower than that in Mnt, which is because the CEC of Ilt is lower than that of Mnt (Zhao and Zhang, 1990). With the increase of temperature, the exchangeable Na^+ and Li^+ in Na^+–Ilt, Li^+–Ilt, and Na^+–Mnt remain almost unchanged. However, exchangeable Li^+ in Li^+–Mnt gradually decrease, indicating that Li^+ is fixed by Mnt upon heating, consistent with the result of XRD.

Table 2. CEC values (mmol/g) of Na^+ and Li^+ in M–Ilt and M–Mnt subjected to varying temperatures.

Temperature (°C)	Na^+ of Na^+-Ilt	Li^+ of Li^+-Ilt	Na^+ of Na^+-Mnt	Li^+ of Li^+-Mnt
25	0.12	0.13	0.74	0.78
100	0.09	0.12	0.73	0.55

https://doi.org/10.1180/mgm.2024.27 Published online by Cambridge University Press

150	0.11	0.13	0.72	0.29
200	0.09	0.11	0.70	0.27
250	0.10	0.12	0.71	0.25
300	0.11	0.12	0.72	0.26

FTIR

To investigate the migration of cations within Ilt and Mnt, mid–infrared spectroscopy was employed to study the shifts in OH group and Si–O vibrational modes. These vibrational modes include stretching and bending vibrations (Liu *et al.*, 2012; Ai *et al.*, 2013; Qi *et al.*, 2022).

OH stretching and bending vibrations

The FTIR spectra of the unheated samples (Na^+–Ilt25, Li^+–Ilt25, Na^+–Mnt25, and Li^+–Mnt25) show a prominent absorption band ~3630 cm^{-1}, attributed to the stretching vibration of the OH group coordinated with the cations in octahedral positions (Fig. 3). The stretching vibrational behavior of the OH group in minerals can be attributed to two factors: 1) the nature of the central atoms in the octahedral coordination with the OH group; 2) the isomorphic substitution in the lattice structure. In this context, the presence of tetrahedral top oxygen (O_{ap}) generates local negative charges, which can be counterbalanced by cations entering the lattice. This interplay influences the OH group's stretching vibrations (Madejová *et al.*, 1999a). During the heating process of Na^+–Ilt, Li^+–Ilt, and Na^+–Mnt samples, the OH stretching vibrational bands remain relatively constant at ~3630

https://doi.org/10.1180/mgm.2024.27 Published online by Cambridge University Press

cm^{-1} (Fig. 3a–c). However, the OH stretching vibrational characteristics of Li^+–Mnt differed noticeably from those of Na^+–Ilt, Li^+–Ilt, and Na^+–Mnt. Upon heating Li^+–Mnt at 100 °C, there is no significant shift in the OH stretching vibration. With further temperature increase, the OH stretching vibrational bands of Li^+–Mnt150, Li^+–Mnt200, Li^+–Mnt250, and Li^+–Mnt300 shift to ~3633, ~3634, ~3638, and ~3641 cm^{-1}, respectively. Previous studies have evidenced that the entry of interlayer cations into the ditrigonal cavities of the tetrahedral layers leads to a shift in OH stretching vibrational bands towards higher wavenumbers (Madejová *et al.*, 2006; Gao, 2017). For Li^+–Mnt25 sample, the interactions between OH and O_{ap} form OH…O_{ap} configurations. Upon cation migration into the ditrigonal cavities the interaction between OH and O_{ap} weakens, while the interaction between O and H in OH strengthens, leading to a shift in stretching vibrations towards higher wavenumbers (Madejová *et al.*, 1999a). Therefore, it is inferred that interlayer Li^+ migrate into the Mnt's ditrigonal cavities when heated to 150 °C.

Notably, a new vibrational band appears in the FTIR spectrum at ~3671 cm^{-1} upon heating Mnt at 200 °C (Fig. 3d). Previous studies have indicated that during the heating process, interlayer hydrated Li^+ could undergo dehydration into the vacant octahedral positions of Mnt, forming a local trioctahedral structure (AlMgLi–OH) and giving rise to the emergence of a

https://doi.org/10.1180/mgm.2024.27 Published online by Cambridge University Press

new OH stretching vibrational band at ~3671 cm^{-1} (Madejová *et al.*, 2006; Jeldres *et al.*, 2019).

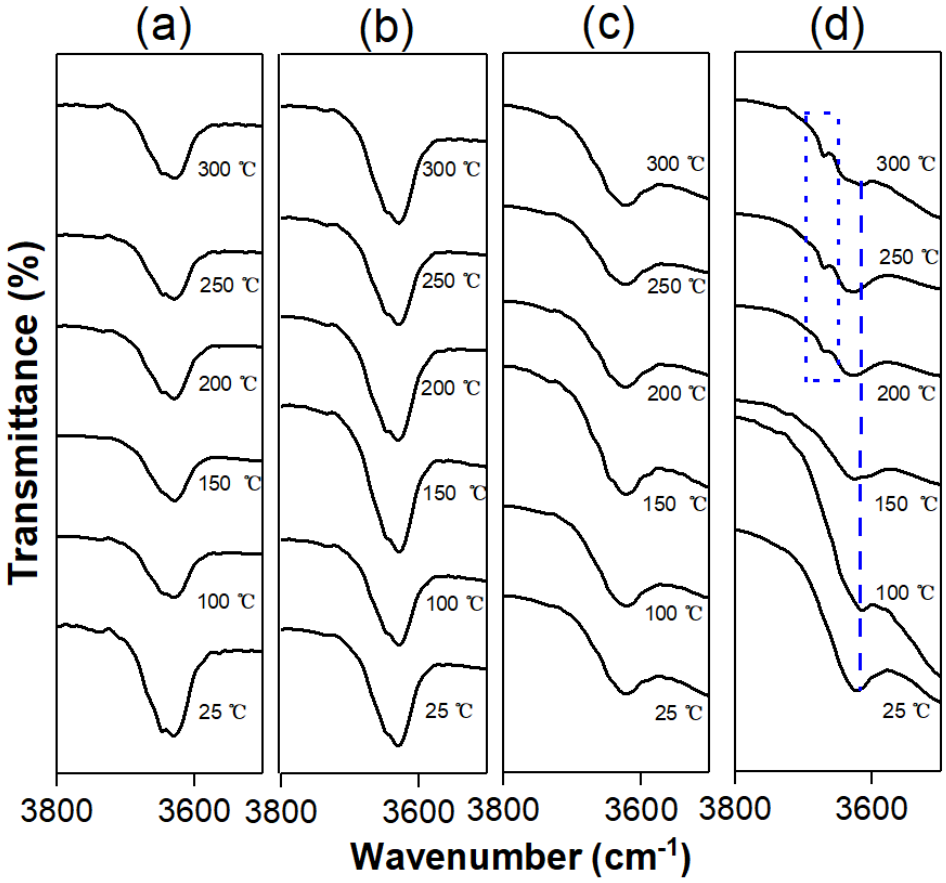

Figure 3. FTIR spectra of OH stretching vibrations: (a) Na^+–Ilt heated at different temperatures; (b) Li^+–Ilt heated at different temperatures; (c) Na^+–Mnt heated at different temperatures; (d) Li^+–Mnt heated at different temperatures.

The characteristics of hydroxyl group bending vibrations provide further insights into the behavior of cation migration during the heating of Ilt and Mnt. The infrared spectra of Na^+–Ilt25 and Li^+–Ilt25 show obvious absorption bands at ~760, ~832, and ~933 cm^{-1} (Fig. 4a,b). Na^+–Mnt25 and Li^+–Mnt25 exhibit pronounced absorption bands at ~797, ~844, and ~912 cm^{-1} (Fig. 4c,d), which are presumed to correspond to OH bending

https://doi.org/10.1180/mgm.2024.27 Published online by Cambridge University Press

vibrations of FeMg–OH, AlMg–OH, and AlAl–OH, respectively, in the mineral structure (Gates *et al.*, 2000; Madejová *et al.*, 2000; Skoubris *et al.*, 2013). The positions and intensities of the OH bending vibrational bands remain unchanged during the heating of Na^+–Ilt, Li^+–Ilt, and Na^+–Mnt samples (Fig. 4a–c). Conversely, for Li^+–Mnt, the OH bending vibrational band corresponding to AlAl–OH is not observed after heating at 150 °C, and the bending vibrational band intensity of OH in AlMg–OH decrease or even disappear with temperature increasing (Fig. 4d), indicating that Li^+ can potentially migrate into the Mnt lattice.

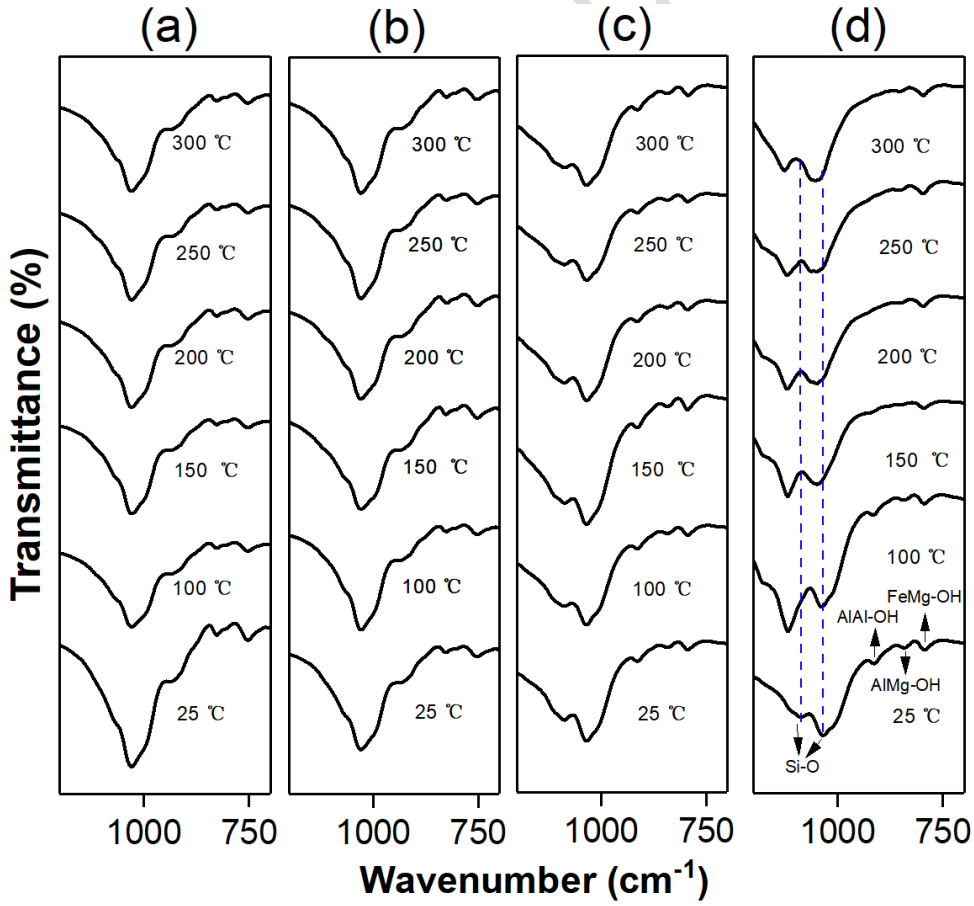

Figure 4. FTIR spectra of OH bending vibrations and Si–O stretching vibrations: (a) Na^+–Ilt heated at different temperatures; (b) Li^+–Ilt heated at different temperatures; (c) Na^+–

https://doi.org/10.1180/mgm.2024.27 Published online by Cambridge University Press

Mnt heated at different temperatures; (d) Li^+–Mnt heated at different temperatures.

As aforementioned, the interlayer cations (Na^+ and Li^+) do not exhibit migration into the Ilt lattice. The Mnt lattice does not accommodate Na^+, but can be migrated by Li^+. This behavior is predominantly influenced by interlayer cation properties, including ionic radius and valence. Specifically, the ionic radii of Na^+ and Li^+ are 0.95 and 0.60 Å, respectively (Madejová *et al.*, 1999a). In comparison to Li^+, Na^+ possesses a larger ionic radius, rendering it less prone to entering the Mnt lattice. Furthermore, the occupation site of Li^+ is not limited to a single location and can include both ditrigonal cavities and vacant octahedral sites. Skoubris *et al.* (2013) reported that upon heating, Mnt undergoes changes in its hydrated Li^+ within the interlayers. These ions dehydrate and transition from interlayer positions to occupy ditrigonal cavities, followed by vacant octahedrons.

Si–O stretching and bending vibrations

The migration of interlayer cations from minerals into ditrigonal cavities of tetrahedral layers leads to changes in Si–O stretching and bending vibrational bands. (Clementz and Mortland, 1974; Alvero *et al.*, 1994). This migration also neutralizes layer charges, rendering Mnt similar to pyrophyllite, a typical uncharged dioctahedral mineral (Karakassides *et al.*, 1999).

Both Na^+–Ilt25 and Li^+–Ilt25 exhibit Si–O stretching vibrational bands

https://doi.org/10.1180/mgm.2024.27 Published online by Cambridge University Press

~1028 cm^{-1} (Fig. 4a,b). Meanwhile, Na^+–Mnt25 and Li^+–Mnt25 display Si–O stretching vibrational bands in the range of 1035–1150 cm^{-1}, with bands at ~1039 and ~1093 cm^{-1}, respectively (Fig. 4c,d). Notably, heated Na^+–Ilt and Li^+–Ilt samples maintain their Si–O stretching vibrational bands, signifying the absence of Ilt's interlayer cations migrating into its lattice structure (Fig. 4a,b). Similarly, the Si–O stretching vibrational bands of Na^+–Mnt remain unchanged during heating, suggesting no migration of interlayer Na^+ into the ditrigonal cavities of Mnt's tetrahedral layers (Fig. 4c). In contrast, Si–O stretching vibrational bands in the Li^+–Mnt series shift to higher values after heating (Fig. 4d). Specifically, the ~1039 cm^{-1} band remains relatively stable at 100 °C; it shifts to a higher value (~1043 cm^{-1}) at 150 °C; it gradually shifts to ~1052 cm^{-1} at 300 °C. This alteration indicates the resemblance of Mnt's structure to that of pyrophyllite, facilitated by Li^+ migration during heating. The Si–O stretching band of pyrophyllite is at ~1050 cm^{-1} (Madejová *et al.*, 2006; Xia *et al.*, 2009). Moreover, the band at ~1093 cm^{-1} shifts to ~1115 cm^{-1} at 100 °C, further shifting to ~1127 cm^{-1} at 200 °C, and eventually progressing to ~1130 cm^{-1} with increasing temperature.

In Ilt, bending vibrational bands of Si–O are mainly located at ~537 (Si–O–Al) and ~484 cm^{-1} (Si–O–Si). These bands' positions and intensities remain largely unchanged as temperature increases (Fig. 5a,b). Mnt's Si–

https://doi.org/10.1180/mgm.2024.27 Published online by Cambridge University Press

O–Si and Si–O–Al bending vibrational bands appear around ~467 and ~520 cm^{-1}, respectively (Fig. 5c,d). The absorption bands of Na^+–Mnt remain constant during heating, whereas the Si–O–Al absorption bands of Li^+–Mnt slightly decrease in intensity with rising temperature.

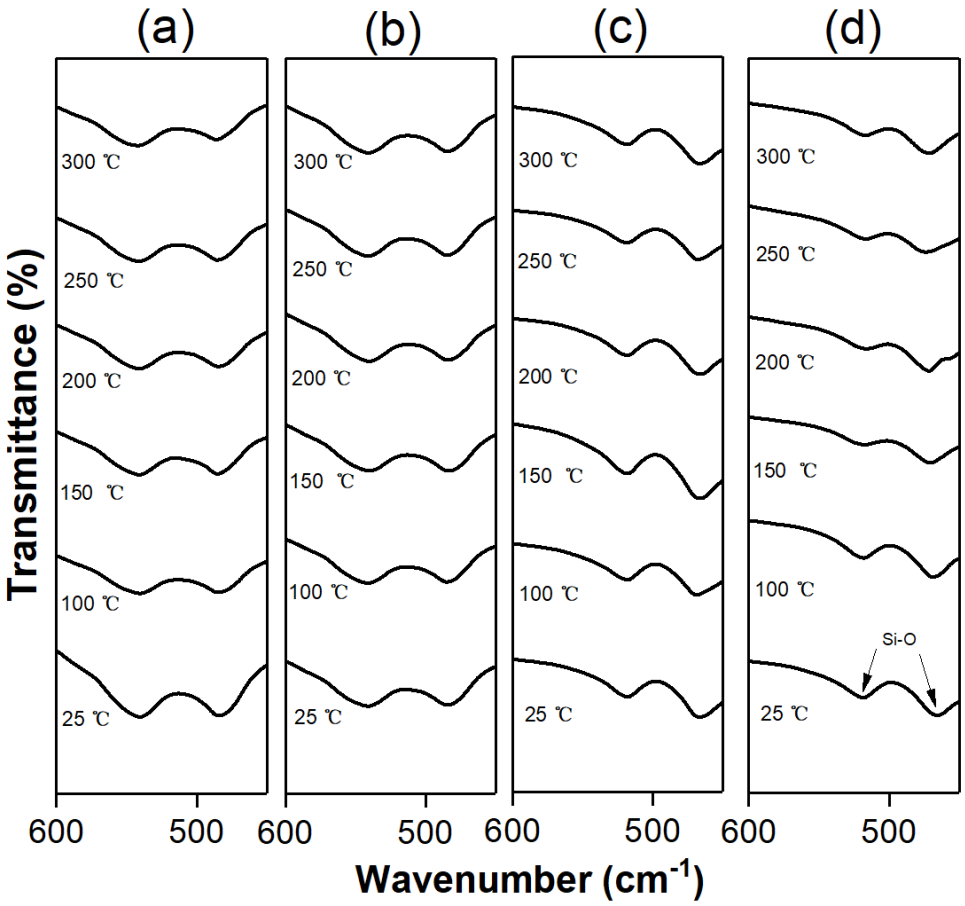

Figure 5. FTIR spectra of Si–O bending vibrations: (a) Na^+–Ilt heated at different temperatures; (b) Li^+–Ilt heated at different temperatures; (c) Na^+–Mnt heated at different temperatures; (d) Li^+–Mnt heated at different temperatures.

In summary, interlayer cations in Ilt do not migrate into its crystal structure. While Na^+ remains within Mnt's interlayers, Li^+ can penetrate ditrigonal cavities of tetrahedral layers.

https://doi.org/10.1180/mgm.2024.27 Published online by Cambridge University Press

MAS NMR and XPS

The XRD and FTIR results indicate that the interlayer Li^+ in Mnt may lose their ligand water when the heating temperature reaches 100 °C, and the interlayer Li^+ migrates into the ditrigonal cavities within the tetrahedral layers when the heating temperature reaches 150 °C. To further demonstrate whether Li^+ can migrate into the vacant octahedral sites of Mnt upon heating to 200 °C, Li^+–Mnt25 and Li^+–Mnt200 were selected for the finer characterization techniques (MAS NMR and XPS).

Fig. 6a illustrates the ^{29}Si–MAS NMR patterns for Li^+–Mnt25 and Li^+–Mnt200 samples. The ^{29}Si signal of Li^+–Mnt25 displays a peak at approximately –92.7 ppm, indicative of tetrahedral silicon atoms connected to three other silicon atoms via oxygen (Alba *et al.*, 1998; Pavón and Alba, 2021). Upon heating to 200 °C, the ^{29}Si signal's peak of Li^+–Mnt200 shifts to approximately –95.3 ppm due to interlayer cations neutralizing negative charges within structural unit layers and integrating into the crystal structure (Steudel *et al.*, 2015). Moreover, the ^{29}Si peak widens, reflecting interlayer cation migration into tetrahedral positions post–heat treatment, leading to Si–O–Si angle changes (Alba *et al.*, 1998). Fig. 6b exhibits ^{27}Al–MAS NMR spectra for Li^+–Mnt25 and Li^+–Mnt200. The ^{27}Al signal in Li^+–Mnt25 appears at ~7.5 and ~67.9 ppm, corresponding to octahedral Al (Al^{VI}) and tetrahedral Al (Al^{IV}), respectively (Takahashi *et al.*,

https://doi.org/10.1180/mgm.2024.27 Published online by Cambridge University Press

2008; Steudel *et al.*, 2015). Additionally, the Al^{IV} signal intensity is notably lower than Al^{VI} due to the higher abundance of Al^{VI} (Reinholdt *et al.*, 2005; Steudel *et al.*, 2015). Post–heating at 200 °C, the Al^{IV} signal disappears, attributed to tetrahedral structure distortion from interlayer Li^+ migration into the lattice (Steudel *et al.*, 2015). Conversely, this effect is less pronounced with Li^+ occupying octahedral vacancies, as a result of minimal interference from a small amount of migrating Li^+ (Steudel *et al.*, 2015). Fig. 6c presents ^{7}Li–MAS NMR spectra of Li^+–Mnt25 and Li^+–Mnt200. Both samples exhibit symmetrical powder sideband patterns, demonstrating a first–order quadrupolar interaction effect (Bodart *et al.*, 2018). For finer crystal structure insight, Fig. 6d shows an enlarged view of ^{7}Li–MAS NMR spectra. The main resonance signal of Li^+–Mnt25 appear at ~0.2 ppm, consistent with interlayer Li^+ (Pistiner and Henderson, 2003). Post–heating to 200 °C, the ^{7}Li signal of Li^+–Mnt200 shifts to approximately –0.6 ppm, indicating octahedral Li^+ presence (Hindshaw *et al.*, 2019).

https://doi.org/10.1180/mgm.2024.27 Published online by Cambridge University Press

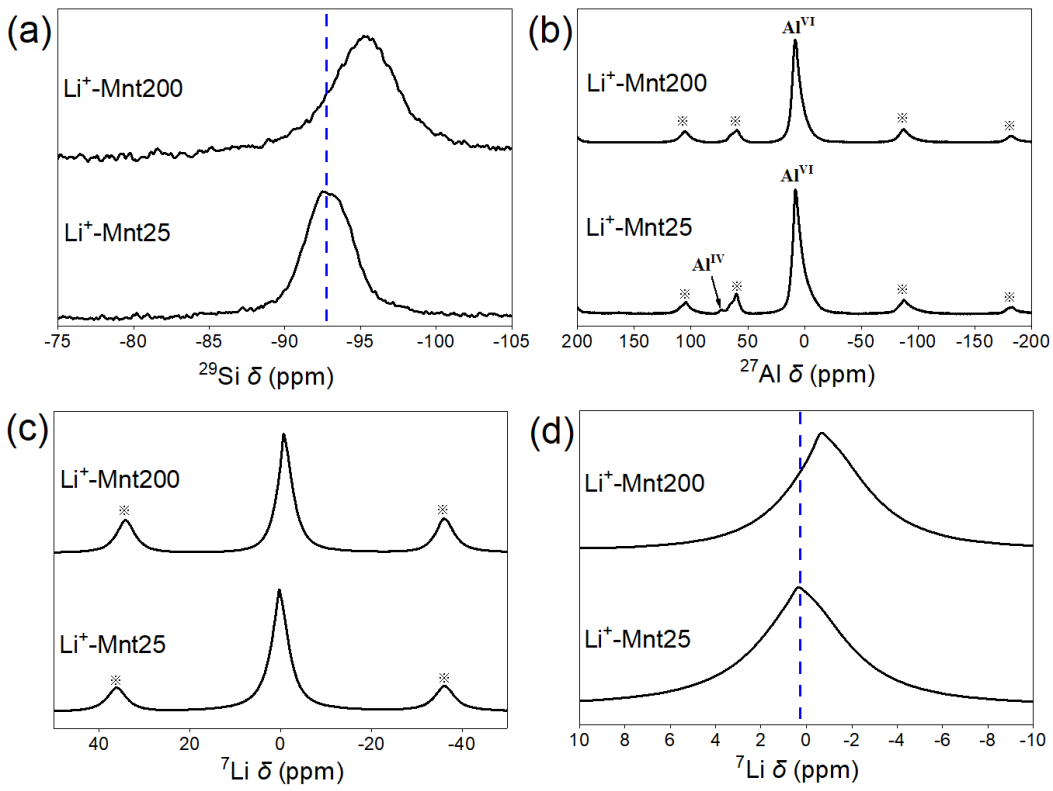

Figure 6. MAS NMR spectra of Li^+–Mnt25 and Li^+–Mnt200: (a) ^{29}Si–MAS NMR spectra; (b) ^{27}Al–MAS NMR spectra, the asterisk indicates spinning sidebands; (c) ^{7}Li–MAS NMR spectra, the asterisk signifies spinning sidebands; (d) Partial amplification from ^{7}Li–MAS NMR spectra.

The XPS spectra depicting Li^+–Mnt25 and Li^+–Mnt200 are presented in Fig. 7. Notably, alterations in the chemical state on the mineral surface significantly influence the positions of the photoelectron peaks. The full spectrum analysis reveals peaks corresponding to O 1*s*, Si 2*p*, and Al 2*p* before and after heating (Fig. 7a). In the case of Li^+–Mnt25, the Si 2*p* peak appears at approximately ~102.7 eV, while after heating to 200 °C, the Si 2*p* peak in Li^+–Mnt200 shifts to ~103.3 eV (Fig. 7b). This shift is attributed to the presumed entry of Li^+ into the ditrigonal cavities of the tetrahedral

https://doi.org/10.1180/mgm.2024.27 Published online by Cambridge University Press

layers, leading to an upwards shift in the Si 2*p* peak. The binding energies of Al 2*p* for Li^+–Mnt25 and Li^+–Mnt200 are situated around ~74.5 and ~75.4 eV, respectively (Fig. 7c). Earlier investigations suggest that the incorporation of Li^+ into the aluminum–oxygen octahedron results in the shift of the Al 2*p* peak towards higher values (Zhong *et al.*, 2021). The Li 1*s* peak in Li^+–Mnt25, located at ~57.3 eV, is hypothesized to represent interlayer hydrated Li^+ (Fig. 7d). Upon heating to 200 °C, the Li 1*s* peaks in Li^+–Mnt200 appear at ~56.2 and ~58.3 eV, respectively (Fig. 7d). This discrepancy indicates that the former peak arises due to the dehydration of a portion of interlayer hydrated Li^+ into Li^+ at elevated temperatures. The latter phenomenon is attributed to the migration of Li^+ into the Mnt lattice, leading to an elevated binding energy of Li 1*s* (Shen *et al.*, 1990; Connell *et al.*, 2020).

https://doi.org/10.1180/mgm.2024.27 Published online by Cambridge University Press

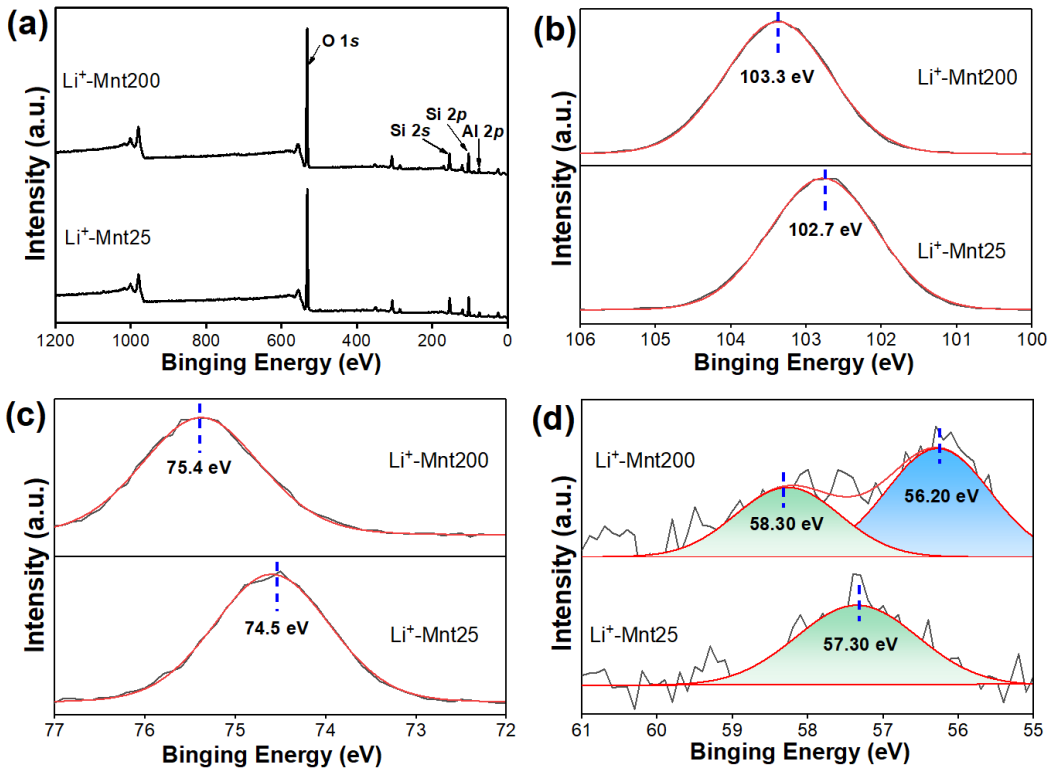

Figure 7. The XPS spectra of Li^+–Mnt25 and Li^+–Mnt200: (a) XPS survey; (b) Si 2*p*; (c) Al 2*p*; (d) Li 1*s*.

Consequently, combined with the emerging OH stretching vibration (AlMgLi–OH) at ~3671 cm^{-1} upon heating Mnt at 200 °C (Fig. 3d), the observed results of MAS NMR and XPS confirm that interlayer Li^+ can migrate to the ditrigonal cavities and vacant octahedral sites of Mnt when heating at 200 °C. In addition, it is explained that when the heating temperature reaches 200 °C, Li^+ can migrate to vacant octahedral sites of Mnt through the ditrigonal cavities.

Migration and occupation of Li^+ in Mnt

Based on XRD, FTIR, MAS NMR, and XPS data concerning the migration and

https://doi.org/10.1180/mgm.2024.27 Published online by Cambridge University Press

occupation of Li^+ in Mnt. This study establishes that Li^+ within the Mnt interlayer can infiltrate the Mnt lattice upon reaching a specific temperature (Fig. 8). This migration of Li^+ occurs through the three–step process. Initially, upon heating to 100 °C, interlayer hydrated Li^+ undergoes dehydration; upon heating to 150 °C, partial Li^+ can migrate into the ditrigonal cavities of the Mnt tetrahedral layers. With further temperature increase to 200 °C, some Li^+ within the ditrigonal cavities proceeds to occupy previously vacant octahedrons in the Mnt, forming a local trioctahedral structure and leading to the complete collapse of the Mnt structural layer (<10.0 Å) (Fig. 8).

https://doi.org/10.1180/mgm.2024.27 Published online by Cambridge University Press

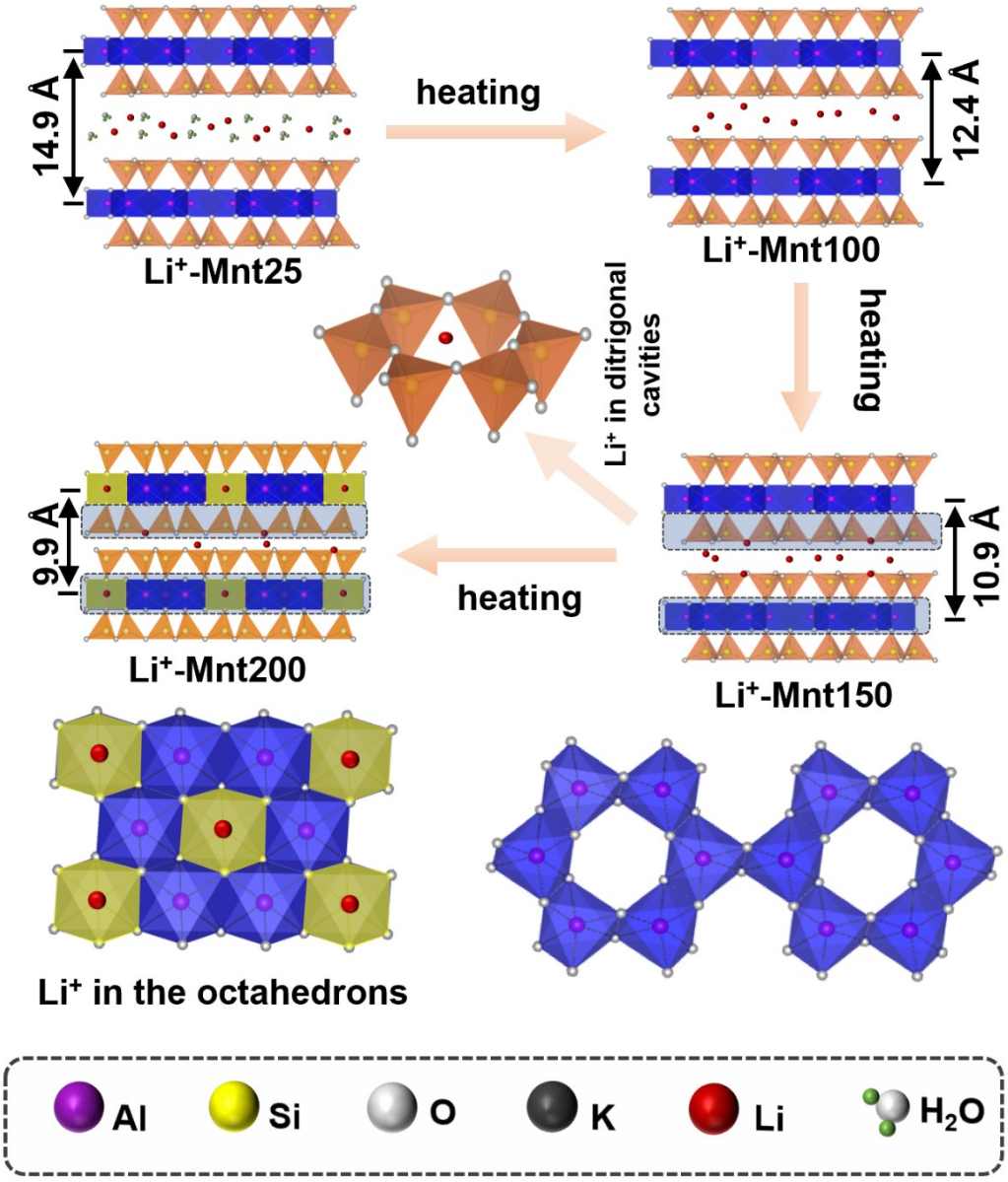

Figure 8. Diagram of Li^+ migration and occupation in Mnt during the heating process.

Conclusions

Under heating conditions, the mineral types and interlayer cations collectively influence the migration and occupation attributes of cations within minerals, thereby impacting mineral lattice structures. In the case of Ilt, the 00*l* reflections exhibit little change after heating, while the $d_{(001)}$

https://doi.org/10.1180/mgm.2024.27 Published online by Cambridge University Press

values of Mnt display pronounced alterations. Specifically, the layer spacing of Li^+–Mnt decreases to less than 10.0 Å, consistent with the complete collapse of Mnt. And exchangeable Li^+ in Li^+–Mnt gradually decrease with the increase of temperature, signifying Li^+ fixation by Mnt. Moreover, within the temperature range of 100–300 °C, the OH vibrational bands and Si–O vibrational bands of Na^+–Ilt, Li^+–Ilt, and Na^+–Mnt remain relatively stable, while those of Li^+–Mnt undergo modifications. Specifically, as the heating temperature reaches 150 °C, the OH stretching and Si–O stretching vibrational bands of the Li^+–Mnt series, shift towards higher values, accompanied by the intensity decrease of OH bending and Si–O bending vibrational bands. These changes are due to the entry of Li^+ into the ditrigonal cavities of Mnt. At 200 °C, the emergence of a new OH stretching vibrational peak around ~3671 cm^{-1} is observed, possibly indicating the entry of Li^+ into Mnt vacant octahedrons and the formation of a local trioctahedral structure (AlMgLi–OH). MAS NMR analysis demonstrates that the chemical shifts of the ^{29}Si and ^{7}Li signals of Li^+–Mnt200 are more negative in comparison to the Li^+–Mnt25 sample. The ^{27}Al–MAS NMR spectrum reveals the disappearance of the Al^{IV} signal upon heating to 200 °C. Furthermore, XPS spectra illustrate that, relative to the Li^+–Mnt25 sample, Al 2*p* and Si 2*p* peaks in Li^+–Mnt200 shift towards higher values, and the Li 1*s* peak emerges at ~58.3 eV. These findings strongly

https://doi.org/10.1180/mgm.2024.27 Published online by Cambridge University Press

support the migration of Li^+ into the crystal structure of Mnt under heating conditions.

Acknowledgment. The authors thank the financial support provided by the National Natural Science Foundation of China (42172043, 42202148) and the Fundamental Research Funds for the Central Universities, CHD (300102263301, 300102273203).

References

Ai Q., Yang Z.J., Zeng X.Q., Zheng Y.L. and Hu P.Y. (2013) Study on the FTIR spectra of OH in olivines from Mengyin Kimberlite. *Spectroscopy and Spectral Analysis*, **33**, 2374-2378 in Chinese with English abstract.

Alba M.D., Alvero R., Becerro A.I., Castro M.A. and Trillo J.M. (1998) Chemical behavior of lithium ions in reexpanded Li-montmorillonites. *The Journal of Physical Chemistry B*, **102**, 2207-2213.

Alvero R., Alba M.D., Castro M.A. and Trillo J.M. (1994) Reversible migration of lithium in montmorillonites. *Russian Journal of Physical Chemistry*, **98**, 7848-7853.

Beaufort D., Berger G., Lacharpagne J.C. and Meunier A. (2001) An experimental alteration of montmorillonite to a di+trioctahedral smectite assemblage at 100 and 200°C. *Clay Minerals*, **36**, 211-225.

Bodart P.R., Delmotte L., Rigolet S., Brendlé J. and Gougeon R.D. (2018) $^{7}Li\{^{19}F\}$ TEDOR NMR to observe the lithium migration in heated montmorillonite. *Applied Clay Science*, **157**, 204-211.

Cao Z., Wang Q. and Cheng H. (2021) Recent advances in kaolinite-based material for photocatalysts. *Chinese Chemical Letters*, **32**, 2617-2628.

Chen T. and Wang H.J. (2007) Microstructure characteristics of illite from Chuanlinggou Formation of Changcheng System in Jixian County, Tianjin City. *Science in China (Series D: Earth Sciences)*, 1452-1458.

Cheng H.F., Yang J., Liu Q.F., Zhang J.S. and Frost R.L. (2010) A spectroscopic comparison of selected Chinese kaolinite, coal bearing kaolinite and halloysite—A mid-infrared and near-infrared study. *Spectrochimica Acta Part A: Molecular and Biomolecular Spectroscopy*, **77**, 856-861.

Clementz D.M. and Mortland M.M. (1974) Properties of reduced charge montmorillonite: Tetra-alkylammonium ion exchange forms. *Clays and Clay Minerals*, **22**, 223-229.

Connell J.G., Fuchs T., Hartmann H., Krauskopf T., Zhu Y.S., Sann J., Garcia-Mendez R., Sakamoto J., Tepavcevic S. and Janek J.r. (2020) Kinetic versus thermodynamic stability of LLZO in contact with lithium metal. *Chemistry of Materials*, **32**, 10207-10215.

Ebina T., Iwasaki T. and Jee A.C. (1999) XPS and DFT study on the migration of lithium in montmorillonite. *Clay science*, **10**, 569-581.

https://doi.org/10.1180/mgm.2024.27 Published online by Cambridge University Press

Farmer V.C. and Russell J.D. (1967) Infrared absorption spectrometry in clay studies. *Clays and Clay Minerals*, **15**, 121-142.

Gao X. (2017) *Clay Mineralogy*. Chemical Industry Press, China: Beijing, 1-230 pp in Chinese with English abstract

Gates W.P., Komadel P., Madejová J., Bujdák J., Stucki J.W. and Kirkpatrick R.J. (2000) Electronic and structural properties of reduced-charge montmorillonites. *Applied Clay Science*, **16**, 257-271.

Gournis D., Lappas A., Karakassides M.A., Többens D. and Moukarika A. (2008) A neutron diffraction study of alkali cation migration in montmorillonites. *Physics & Chemistry of Minerals*, **35**, 49-58.

Greene-Kelly R. (1995) Dehydration of the montmorillonite minerals. *Mineralogical Magazine and Journal of the Mineralogical Society*, **30**, 604-615.

Hindshaw R.S., Tosca R., Goût T.L., Farnan I., Tosca N.J. and Tipper E.T. (2019) Experimental constraints on Li isotope fractionation during clay formation. *Geochimica Et Cosmochimica Acta*, **250**, 219–237.

Jeldres R.I., Uribe L., Cisternas L.A., Gutierrez L., Leiva W.H. and Valenzuela J. (2019) The effect of clay minerals on the process of flotation of copper ores - A critical review. *Applied Clay Science*, **170**, 57-69.

Karakassides M.A., Madejová J., Arvaiová B., Bourlinos A., Petridis D. and Komadel P. (1999) Location of Li(I), Cu(II) and Cd(II) in heated montmorillonite: evidence from specular reflectance infrared and electron spin resonance spectroscopies. *Journal of Materials Chemistry*, **9**, 1553-1558.

Komadel P., Madejova J. and Bujdak J. (2005) Preparation and properties of reduced-charge smectites—A review. *Clays and Clay Minerals*, **53**, 313-334.

Li R.H., Li X.Y., Li H.R., Zhao K.P. and Peng K. (2022) Structural characteristics of clay minerals and their progress in CO_2 adsorption. *Bulletin of the Chinese Ceramic Society*, **41**, 141-152 in Chinese with English abstract.

Liu Q.F., Yao X., Cheng H.F. and Frost R.L. (2012) An infrared spectroscopic comparison of four Chinese palygorskites. *Spectrochimica Acta Part A: Molecular and Biomolecular Spectroscopy*, **96**, 784-789.

Luca V. and Cardile C.M. (1988) Thermally induced cation migration in Na and Li montmorillonite. *Physics and Chemistry of Minerals*, **16**, 98-103.

Madejová J., Arvaiová B. and Komadel P. (1999a) FTIR spectroscopic characterization of thermally treated Cu^{2+}, Cd^{2+}, and Li^{+} montmorillonites. *Spectrochimica Acta Part A*, **55**, 2467-2476.

Madejová J., Arvaiová B. and Komadel P. (1999b) FTIR spectroscopic characterization of thermally treated Cu^{2+}, Cd^{2+}, and Li^{+} montmorillonites. *Spectrochimica Acta Part A: Molecular and Biomolecular Spectroscopy*, **55**, 2467-2476.

Madejová J., Bujdák J., Petit S. and Komadel P. (2000) Effects of chemical composition and temperature of heating on the infrared spectra of Li-saturated dioctahedral smectites. (I) Mid-infrared region. *Clay Minerals*, **35**, 739-751.

Madejová J., Pálková H. and Komadel P. (2006) Behaviour of Li^{+} and Cu^{2+} in heated montmorillonite: Evidence from far-, mid-, and near-IR regions. *Vibrational Spectroscopy*, **40**, 80-88.

Pavón E. and Alba M.D. (2021) Swelling layered minerals applications: A solid state NMR overview. *Progress in Nuclear Magnetic Resonance Spectroscopy*, **124-125**, 99-128.

Pistiner J.S. and Henderson G.M. (2003) Lithium-isotope fractionation during continental weathering processes. *Earth and Planetary Science Letters*, **214**, 327-339.

Qi C.W., Yin Y.S., Wu Z.H., Tao J.H., Wang T., Cheng S., Liu L. and Chen D.L. (2022) Study on mineral transformation during the combustion of Xiangxi Coal by FTIR, XRD and XPS. *Coal Conversion*, **45**, 18-25 in Chinese with English abstract.

https://doi.org/10.1180/mgm.2024.27 Published online by Cambridge University Press

Reinholdt M., Miehe-Brendle J., Delmotte L., Le Dred R. and Tuilier M.H. (2005) Synthesis and characterization of montmorillonite-type phyllosilicates in a fluoride medium. *Clay Minerals*, **40**, 177-190.

Russell J.D. and Farmer V.C. (1964) Infrared spectroscopic study of the dehydration of montmorillonite and saponite. *Clay Minerals Bulletin*, **5**, 443-464.

Schultz L.G. (1969) Lithium and potassium absorption, dehydroxylation temperature, and structural water content of aluminous smectites. *Clays and Clay Minerals*, **17**, 115-149.

Shen M.L., Hrbek J., Sham T.K. and Xu G.Q. (1990) A soft X-ray study of the interaction of oxygen with Li. *Surface Science*, **234**, 324-334.

Skoubris E.N., Chryssikos G.D., Christidis G.E. and Gionis V. (2013) Structural characterization of reduced-charge montmorillonites. Evidence based on FTIR spectroscopy, thermal behavior, and layer-charge systematics. *Clays and Clay Minerals*, **61**, 83-97.

Stackhouse S. and Coveney P. (2002) Study of thermally treated lithium montmorillonite by Ab Initio methods. *Journal of Physical Chemistry B*, **106**, 12470-12477.

Steudel A., Heinzmann R., Indris S. and Emmerich K. (2015) CEC and ^{7}Li MAS NMR study of interlayer Li^{+} in the montmorillonite-beidellite series at room temperature and after heating. *Clays and Clay Minerals*, **63**, 337-350.

Takahashi T., Kanhhashi K. and Saito K. (2008) First evidence of multiple octahedral Al sites in Na-montmorillonite by ^{27}Al multiple quantum MAS NMR. *Clays and Clay Minerals*, **56**, 520-525.

Tettenhorst R. (1962) Cation migration in montmorillonites. *American Mineralogist*, **47**, 769-773.

Theng B.K.G., Hayashi S., Soma M. and Seyama H. (1997) Nuclear magnetic resonance and X-ray photoelectron spectroscopic investigation of lithium migration in montmorillonite. *Clays and Clay Minerals*, **45**, 718-723.

Wang J., Wang J.X., Zeng F.G. and Wu X.L. (2011) Molecular simulations of crystal structure conformation, X-ray diffraction and infra-red spectrum in montmorillonites. *Acta Mineralogica Sinica*, **31**, 133-138 in Chinese with English abstract.

Wu Z., Zhao H., Zhou X., Wang Y., Zuo K. and Cheng H. (2022) Thermal Migration Behavior of Na^{+} , Cu^{2+} and Li^{+} in Montmorillonite. *Minerals*, **12**, 477.

Xia L.Y., Zhong H., Liu G.Y., Huang Z.Q., Chang Q.W. and Li X.G. (2009) Comparative studies on flotation of illite, pyrophyllite and kaolinite with Gemini and conventional cationic surfactants. *Transactions of Nonferrous Metals Society of China*, **19**, 446-453+442.

Zhao H., Wang Y. and Cheng H.F. (2023) Recent advances in lithium extraction from lithium-bearing clay minerals. *Hydrometallurgy*, **217**, 106025.

Zhao K., Li G.R., Sun Z.X., Liu J.H., Zhou Y.P. and Xu L.L. (2022a) Role of clay minerals in uranium mining and metallurgy and uranium rich environment treatment. *Nonferrous Metals (Extractive Metallurgy)*, 111-120 in Chinese with English abstract.

Zhao X.Y. and Zhang Y.Y. (1990) *Analysis of Clay mineral and Clay mineral*. China Ocean Press, Beijing

Zhao Y., Ma W.P., Yang Y., Cui Y., Xu L., Luo C.G. and Wen H.J. (2022b) Experimental study on the sorption of Li^{+} by clay minerals—implications for clay-type lithium deposit. *Acta Mieralogica Sinica*, **42**, 141-153 in Chinese with English abstract.

Zhong J., Lin S. and Yu J.G. (2021) Li^{+} adsorption performance and mechanism using lithium/aluminum layered double hydroxides in low grade brines. *Desalination*, **505**, 114983.

https://doi.org/10.1180/mgm.2024.27 Published online by Cambridge University Press